Gisbert-González, JM.; Cheuquepán, W.; Ferre Vilaplana, A.; Herrero, E.; Feliu, JM. (2020). Citrate adsorption on gold: Understanding the shaping mechanism of nanoparticles. Journal of Electroanalytical Chemistry. 875:1-11. https://doi.org/10.1016/j.jelechem.2020.114015

Citrate adsorption on gold: understanding the shaping mechanism of nanoparticles.

José M. Gisbert-González[a], *William Cheuquepán*[a], *Adolfo Ferre-Vilaplana*[b]*, *Enrique Herrero*[a]*, *Juan M. Feliu*[a]

[a]Instituto de Electroquímica, Universidad de Alicante, Apdo. 99, E-03080 Alicante, Spain.

[b]Instituto Tecnológico de Informática, Ciudad Politécnica de la Innovación, Camino de Vera s/n, E-46022 Valencia, Spain, and Departamento de Sistemas Informáticos y Computación, Escuela Politécnica Superior de Alcoy, Universidad Politécnica de Valencia, Plaza Ferrándiz y Carbonell s/n, E-03801 Alcoy, Spain.

Abstract

Advanced applications of colloidal nanoparticles (NPs) become to depend on their specific shape, which is controlled by the adsorption behavior of the capping agent involved in their synthesis. To understand the way in which citric acid determines the shape of gold NPs, the adsorption behavior of citrate on gold under the synthesis conditions is here investigated from electrochemical experiments on well-defined surfaces. Gibb excesses and charge numbers for the citrate adlayers deposited on the Au(111), Au(100) and Au(110) electrodes when a potential is applied were estimated at pHs 1 and 3. From these results, FTIR spectra and DFT calculations, it is concluded that solvated citrate can become simultaneously adsorbed through three dehydrogenated carboxylic groups in bidentate configuration on Au(111), but only through two on Au(100) and Au(110). As a result of this behavior, citrate can become more strongly adsorbed on Au(111) than on the other two basal planes of gold under the synthesis conditions, which would explain why tetrahedral and octahedral colloidal gold NPs are preferentially shaped when citric acid is used as the capping agent in water. This conclusion coincides with the previously one obtained on platinum, suggesting that the mechanism here described would operate also on other metals having fcc structure.

1. Introduction.

The shape of metal nanoparticles (NPs) is connected to the symmetry of the crystalline surfaces exposed by their faces. Thus, advanced applications of metal NPs require not only size but also shape control. Optimal in shape and size metal NPs (usually platinum) allow to enhance the activity of a given load of catalyst in fuel cells [1]. And, optimal in shape and size biocompatible metal NPs (mainly gold) can be functionalized to selectively link them to specific biological receptors with extraordinary selectivity [2-5]. Once linked to their targets, the selective optical excitation of the NPs can drive advanced per image diagnostic procedures. The thermalization of such a kind of specific excitations enables the localized treatment of tumors and infectious diseases. And, the selective adsorption of active principles on the specific surfaces exposed by the NPs allows selective drug delivery [2-5]. Thus, methods of producing metal NPs having specific shape and size are enabling technologies in Nanomedicine and Nanotecnology.

In recent years, procedures for obtaining colloidal metal NPs with a preferential shape, exposing surfaces having a dominant symmetry, have been developed [6-12]. To this end, citric acid (2-hydroxypropane-1,2,3-tricarboxylic acid) has been extensively employed, not only as a mild reductive agent, but also as capping agent to produce nanoparticles with a preferential shape. Citric acid presents some advantages with respect to other shaping agents, such as biocompatibility in physiological environments and low cost. Thus, different processes using this molecule as the capping agent have been reported. Among them, the Turkevich method is the most commonly employed for gold (AuNPs) in water [13], which was further refined by Frens et al [14].

The currently available colloidal synthesis methods of metol NPs are mainly the result of trial-and-error procedures. However, mechanistic knowledge of the way in

which capping agents shape metal NPs could boost the engineering of future methods and shaping agents. Several works report on the citrate adsorption on the Au(111) surface [15, 16]. Scanning tunneling microscopy (STM) studies show that adsorbed citrate species forms a stable and well-ordered adlayers exhibiting ($4 \times 2\sqrt{3}$) symmetry on Au(111) [17]. The nature of the adsorbed species has been identified using in situ subtractive normalized interfacial Fourier transform infrared spectroscopy (SNIFTIRS). The spectra are compatible with citrate species adsorbed through deprotonated carboxylic groups oriented tilted with respect the surface normal [18]. Moreover, thermodynamic studies at pH=1 points to a maximum citrate coverage of 3×10^{-10} mol cm^{-2} on Au(111) (equivalent to 1.8×10^{14} ion cm^{-2}), and to electrosorption valency and reciprocal of the Esin-Markov coefficient greater than 2, at high surface densities [19]. However, the citrate adsorption on the other two basal planes of gold (Au(100) and Au(110)) has not yet been characterized, reason why the shaping mechanism of citrate on gold has not yet been completely untangled.

Here we report on the citrate adsorption on Au (111), Au (100) and Au (110) single crystal electrodes. Through a set of electrochemical experiments, FTIR spectra and DFT calculations on well-defined surfaces, the adsorption behavior of citrate on the three basal lanes of gold is unequivocally characterized. From these results, the shaping mechanism of citrate on gold in water is proposed.

2. Experimental and computational methods.

2.1. Experimental methods

Au(hkl) single crystal electrodes were prepared using the Clavilier procedure for platinum [20], which has been extended to other noble metals. Single crystal beads were obtained by fusion and subsequent crystallization of an ultrapure 0.5 mm diameter

gold wire. After careful cooling, these beads were mounted in a four-cycle goniometer on an optical bench, oriented using the reflection of a laser, and cut and polished along the desired orientation. Before their use, they were flame annealed and cooled down with water, keeping a protective droplet in equilibrium with the atmosphere.

A 25 nm-thick gold thin film (99.999%, Kurt J. Lesker Ltd.) thermally evaporated on one of the faces of a low oxygen-content silicon prism beveled at 60º (Pastec Ltd, Japan) was used as working electrode in the internal reflection infrared spectroscopy experiments (ATR-SEIRAS). Deposition was carried out in the vacuum chamber of a coating system (PVD75, Kurt J. Lesker Ltd.) at a base pressure around 10^{-6} Torr using a quartz crystal microbalance to control both the thickness of the gold film and the deposition rate (fixed at 0.006 nm s^{-1}). Once in the spectroelectrochemical cell, the gold thin film electrodes were cleaned by applying a few voltammetric cycles up to the onset of surface oxidation in the 0.1 M $HClO_4$ solution. Then, sodium acetate was added up to a 10 mM concentration to the working solution and an electrochemical annealing of the electrode surface was carried out by cycling the electrode potential at 20 $mV \cdot s^{-1}$ between 0.05 and 1.10 V for one hour [21]. Subsequently, the spectroelectrochemical cell was thoroughly flushed with a 0.1 M $HClO_4$ until acetate anions were removed. Based on the preferential (111) orientation of the samples obtained with this procedure [22], the previously used Au(111)-25nm notation [23] will also be employed in this work.

All the voltammetric and in situ infrared experiments were performed in glass cells using a reversible hydrogen electrode (RHE) for pH=1 solutions, a $Ag/AgCl_{sat}$ electrode (which has been converted to RHE scale for data comparison for pH=3) as reference electrodes and a gold wire as the counter electrode. Working solutions were prepared from, citric acid (≥99.5% Sigma-Aldrich), concentrated perchloric acid (Merck

Suprapur®) and ultrapure water (18.2 MΩ·cm, TOC 50 ppb max, Elga Vivendi). In some experiments, solutions were prepared in deuterium oxide (99% D, Aldrich), which was used as received. Solutions were deaerated with Ar (N50, Air Liquide) and blanketed with this gas during the experiments. Voltammetric experiments were carried out with a Wave signal generator (EG&G PARC 175), potentiostat (eDAQ 161), and digital recorder (eDAQ e-corder 401) workstation. All experiments were carried out at room temperature.

In situ infrared experiments were carried out with a Nexus 8700 (Thermo Scientific) spectrometer equipped with a MCT-A detector and a wire grid ZnSe polarizer (Pike Tech). The spectroelectrochemical cell [24], equipped with a Si (ATR-SEIRAS) window beveled at 60º, was placed at the top of a Veemax (Pike Tech.) reflectance accessory. All the potential-dependent spectra were collected with a resolution of 8 cm^{-1} and are presented in absorbance units (a.u.) as $-\log(R/R_o)$, where R and R_o represent the reflectivities at the sample and reference potentials, respectively. Thus, positive and negative bands correspond to gain and loss of species at the sample potential with respect to the reference potential, respectively. In most of the experiments, the electrode potential was stepped from the reference to the sample potential collecting 100 interferograms at each potential. All the spectra are referred to the reference single beam spectrum obtained in the citrate or citric acid containing solutions at 0.10 V. Cyclic voltammograms were recorded at ν=20 mV s^{-1}.

2.2. Computational methods

All DFT calculations were carried out using numerical basis sets [25], semi-core pseudopotentials [26] (which include scalar relativistic effects) and the PBE [27] and RPBE [28] functionals as implemented in the $Dmol^3$ code [29]. When considered,

dispersion forces were corrected by the Tkatchenko and Scheffler method [30]. Continuous solvation effects were taken into account by the COSMO model [31]. The effects of non-zero dipole moments, in the supercells, were canceled by means of external fields [32]. Proton-coupled electrons transfers were modeled by means of the computational hydrogen electrode formalism [33].

Being specifically developed for catalysis, it is generally assumed that RPBE provides a better description of adsorption on transition metals than PBE. In fact, it is known that PBE systematically over-bind regarding RPBE. Moreover, due to the size of the investigated adsorbate, it can be anticipated that the effect of the dispersion forces could become significant. However, the treatment of the dispersion forces under the RPBE functional is not supported by the aforementioned software package. In order to obtain dispersion corrected RPBE results, dispersion corrected PBE results were in turn corrected by the difference between dispersion uncorrected PBE and RPBE results. Constant lattices were specifically estimated for each numerical treatment, that is, PBE, RPBE, and PBE-D, and the corresponding one was used in the assembling of each model.

The Au(111), Au(100) and Au(110) surfaces were modeled by means of periodic supercells comprising 48 Pt atoms (four layers of metal atoms) and a vacuum slab of 20 Å. The bottom 24 Au atoms were frozen in their bulk crystal locations, meanwhile, the remaining 24 Au atoms were completely relaxed joint to the adsorbates. The shortest distance between periodic images was in the order of 8.90 Å for all the models. Additional details, about the computational methods, are provided in [16].

3. Results and discussions

3.1. Citrate adsorption on gold from experiments

3.1.1. Citrate adsorption on the Au(111) electrode

Insights into the citrate adsorption behavior on the Au(111) surface in water can be derived from the voltammetric profiles displayed in Figure 1, obtained at different citric acid concentrations under pHs 1 (0.1 M $HClO_4$) and 3 (2.99×10^{-2} M $HClO_4$+ 4.84×10^{-2} NaF). Since the thermodynamic analysis that will be employed later requires that the total ionic strength and the pH is kept constant (so that the activity coefficients are also constant) citric acid was used to increase the total concentration of citrate species in solution. The presence of citric acid in solution gives rise to the appearance of a complex voltammetric signal related with the citrate adsorption process between 0.23 and 1.2 V. At low potentials, the Au(111) surface is reconstructed, forming a ($22\times\sqrt{3}$) structure (also termed as herringbone structure) [34-36]. Under this reorganization, the adsorption of citrate leads to the lifting of the reconstruction, which is marked by the sharp spike at ca. 0.70 V for pH=1 and the lowest citrate concentration [37]. As can be seen, the potential for this process diminishes as the citrate concentration increases, in a similar way to the behavior observed for other adsorbed anions such as sulfate [37-39]. Finally, at ca. 1.2 V, just before the onset for the oxidation of the surface, the measured current is similar to that observed in the absence of citrate, signaling the almost completion of the adlayer. However, the measured current for the different concentrations of citrate at 1.2 V is not the same, which suggests that the adlayer might not be fully completed when the surface oxidation starts. As the citric acid concentration increases, the citrate adsorption wave shifts to lower potential values, in a similar way to what is observed for sulfate [40-42]. Regarding the pH effect, the curves for pHs 1 and 3 are very similar, with similar onset potential for the adsorption of citrate in the

RHE scale. Additionally, the lifting of the reconstruction takes place at comparable values, which also corroborates that this lifting is triggered by a given citrate coverage.

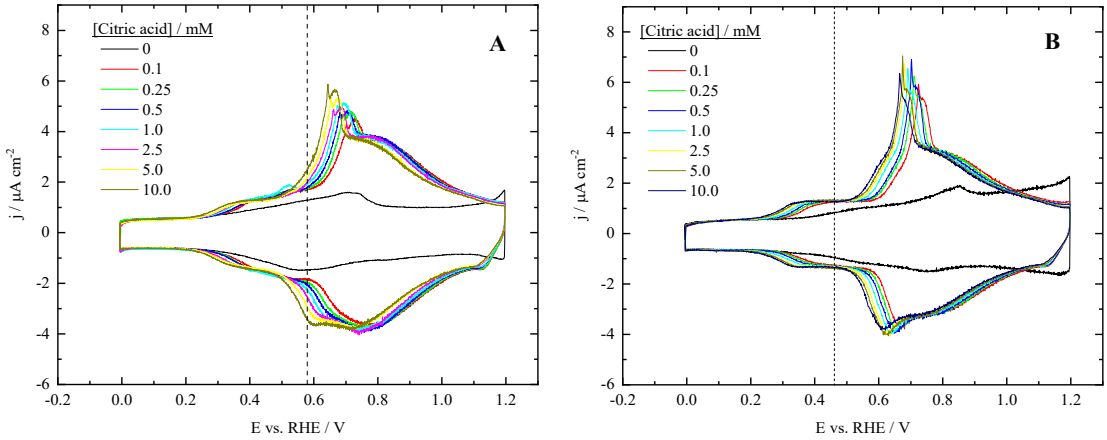

Figure 1 Voltammetric profiles of the Au(111) electrode at different citric acid concentrations under A) 0.1 M $HClO_4$ (pH=1.2) and B) 2.99×10^{-2} M $HClO_4$+ 4.84×10^{-2} NaF (pH=2.9) conditions. Scan rate 20 mV s^{-1}. The vertical line marks the position of the pzc of the unreconstructed surface.

When the scan is reversed, the voltammetric profile is not symmetrical with respect to the potential axis, because the surface reconstruction is a slow process. Unlike the lifting process, which is fast and readily triggered by the citrate coverage, the reconstruction process requires potentials below 0.3 V and enough time to reach a significant extension [41, 42]. Furthermore, continuous cycling of the electrode tends to maximize the unreconstructed-surface dominance, and the reconstructed surface is only fully restored by maintaining the electrode at low potential for long periods, as has been already reported on the Au(100) electrode [43]. Sine the relevant signals corresponding to citrate adsorption in the negative scan direction are observed at potentials higher than that required to trigger the formation of the reconstructed surface, it can be considered that the signals corresponds mainly to adsorption processes in the (1×1) surface of the Au(111) electrode [44], although provably some interference in the lower potentials values is always possible.

To calculate the citrate surface excesses and the electrosorption valency, a thermodynamic analysis using the electrocapillary equation can be employed. In order

to do that, the surface structure should be identical for the initial and final state, to avoid interferences in the analysis due to changes in the reconstruction. As aforementioned, only the negative scan direction can be used, which corresponds to desorption from a (1×1) surface. It can be considered that, during the desoprtion time, the extension of the reconstruction giving rise to the herringbone structure is almost negligible. Using the same procedure as that employed for the adsorption of citrate on the Pt(111) electrode [16] (summarized in the supporting information), charge densities can be obtained by the integration of the current measured in the negative scan direction. Since the potential of zero charge (pzc) for the supporting electrolyte are known, being 0.55 and 0.47 V vs. SHE for the (22×√3) and (1×1), respectively [44-46], the latter value was used as an integration constant, assigning zero as value for the charge at this potential. In Figure 1, the position of the pzc for each pH has been marked by a vertical dashed line. Since the presence of citrate should shift the pzc to negative values, the charge at 0.47 V is dependent on the citrate concentration. However, the charge at the lower limit (0 V) should be the same for all the citrate concentrations, given that citrate has been completely desorbed. Thus, the charge value measured at 0 V in the supporting electrolyte was used as integration constant for all the citrate-containing curves.

The charge density curves for citrate in different solutions at pHs 1 and 3, displayed in Figure S1, are very similar to those observed for other anions [40, 47-50]. At low potentials, these curves for different concentrations overlap, since there is no citrate adsorption at these values. After the onset potential for the adsorption, the curves are different for different concentrations, which should finally eventually converge, at high potentials, when the adlayer has been completed (defined as that reaching the maximum coverage). However, as can be seen, such a kind of convergence is not

reached on the Au(111) surface, implying that the adlayer has not reached its completion at the upper potential, as suggested by the voltammetric behavior.

From these charge density curves, and using the procedure described in the supporting information, values for the difference in the Parsons function at a given potential and that measured at the potential of zero charge, $\xi - \xi_{\sigma_M=0}$ (figure S4) and, from that, surface excesses for citrate species can be calculated (Figure 2). It should be highlighted that the calculated excesses accumulate the excesses of all the possible citrate species in the adlayer: citric acid, dihydrogen citrate, monohydrogen citrate and citrate. The maximum excess calculated for citrate at pH=1 (Figure 2A) is 2.8×10^{14} ions cm^{-2}, which is consistent with the previous observation that complete adlayers are not formed on the Au(111) surface before surface oxidation. If the adlayer would be complete, the excess would probably be very close to 3×10^{14} ions cm^{-2}, which corresponds to a surface coverage of 0.2. This value is also the maximum surface coverage for adsorbed sulfate on Au(111) [40] and adsorbed citrate on Pt(111) [16]. For pH=3 (Figure 2B), the shape of the citrate excess curves is very similar to that obtained for pH=1, though the maximum coverage at 1.2 V is close to 3×10^{14} ions cm^{-2}, higher than that obtained for pH=1, which was also found by Lipkowski et al. [19]. It is important to highlight that the calculated Gibbs excesses are quasi-independent of the citrate concentration in the potential range 0.280 V < E < 0.540 V for pH 1, which suggest that the interaction of the citrate species with the surface at low coverages for this pH value is different from that taking place at higher coverages. Thus, the initial interaction of citrate with the surface does not follow the typical behavior of adsorbed anions.

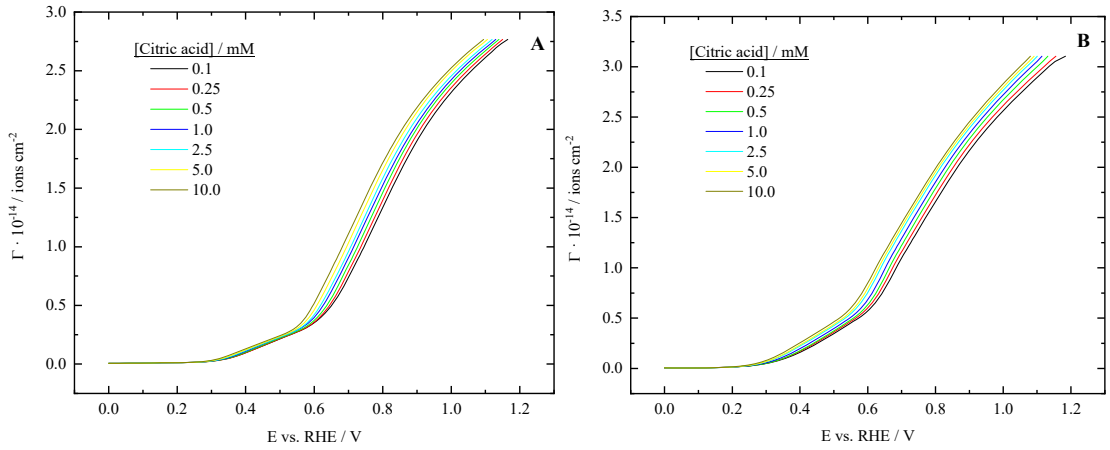

Figure 2. Gibb excess vs. Potential of the Au(111) electrode in different solutions A) 0.1 M $HClO_4$ (pH=1.2); B) 2.99×10^{-2} M $HClO_4$+ 4.84×10^{-2} NaF (pH=2.9); under different citric acid concentrations. Scan rate 20 mV s^{-1}. The vertical line marks the position of the pzc of the unreconstructed surface.

When the citrate adsorption process on Au(111) is compared with that on Pt(111), some important differences can be observed. First, the potential window under which citrate adsorption takes place is significantly smaller on Pt. From the onset potential, only ca. 250 mV are required to complete the adlayer on platinum, whereas more than ca. 1 V is required on gold. This fact implies that the specific interaction of the citrate species with the surface is significantly weaker for gold. On the other hand, the pH effect on the adsorption process is also different. The excess vs. electrode potential curves in the RHE scale are practically pH independent on platinum, whereas the obtained excess are slightly higher at pH=3 than at pH=1 for a given potential on gold (Figure 3A). To achieve a given surface excess, the required potential in the RHE scale is ca. 60 mV lower for pH=3 than for pH=1, which implies that the process shifts ca. 180 mV to more negative values in the SHE scale, when changing 2 pH units. This number implies protons to exchanged electrons ratio 3/2. Thus, the proposed citrate adsorption reaction would be:

$$Au + C_6H_8O_7 \rightarrow Au\text{-}C_6H_5O_7^- + 3H^+ + 2e^- \qquad (1)$$

In this reaction, the negative charge of the adsorbed citrate is counterbalanced with Na^+ ions, so that adsorbed species is neutral.

To corroborate this equation, the charge numbers for the adsorption reaction were calculated (Figure 3B). The value 2 was obtained for the central region of the potential window where the adsorption takes place, which is consistent with the proposed equation. Significant deviations from this value at low coverages would be due to measurement errors. At low coverages, the relative error in the calculated excess is higher, which leads also to large errors in the charge numbers. It is worth highlighting that the proposed adsorption equation for gold (equation (1)) is different from that proposed for platinum [16], given that citrate is completely discharged upon adsorption on Pt(111) (i.e., with a charge number close to 3), whereas adsorbed citrate retains some negative charge in the adsorbent/adsorbate complex on Au(111). This difference in the charge state explains why the potential window for these adsorption processes are so different on Pt(111) and Au(111). This behavior is connected with the stronger interaction of the citrate species with platinum. Finally, the fact that adsorbed citrate retains some negative charge, giving rise to repulsive interactions among neighboring adsorbed citrate species, also explains why complete citrate adlayers are not deposited on Au(111) before the onset of surface oxidation.

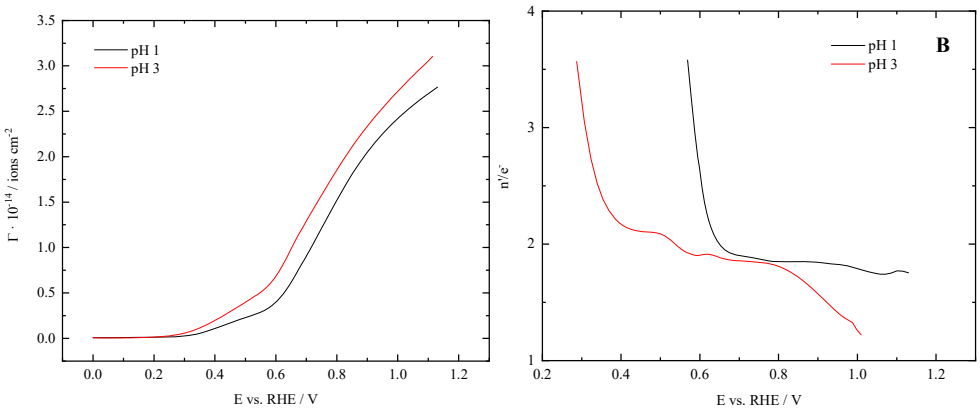

Figure 3. A) Gibb excesses and B) charge number vs. potential at different pH under 10^{-3} M citric acid.

3.1.2. Citrate adsorption on the Au(100) electrode.

Surface excesses and charge numbers were also determined on the Au(100) electrode, using the previously applied procedure. The corresponding voltammograms at pHs 1 and 3 for the different citrate concentrations are displayed in Figure 4. Between 0.2 and 1.2 V, a voltammetric wave related to citrate adsorption emerges with a maximum around 0.6-0.7 V. On to top of this wave, the characteristic peak associated with the lifting of the surface reconstruction from the Au(100)-hex to the (1x1) surface is clearly visible [38, 51-53]. As expected, increasing the citrate concentration moves the adsorption/desorption states and the reconstruction peak to more negative potential, reducing the stability of the reconstructed surface [54]. The effect of the pH in the voltammogram shape is almost negligible. The only minor change is the appearance of a shoulder above 0.4 V at pH 3, which can be related to a change in the electrode surface charge under these conditions, as happens on Au(111).

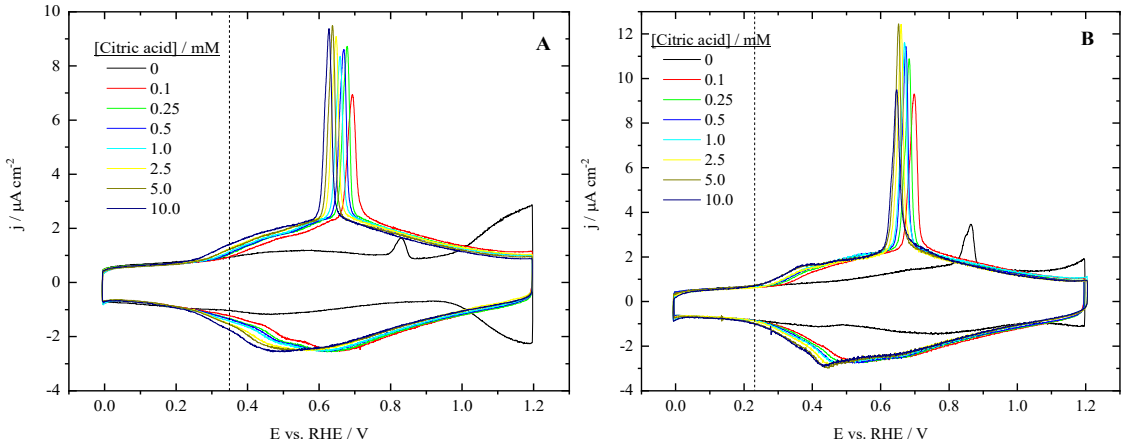

Figure 4. Voltammetric profiles of the Au(100) electrode in different solutions A) 0.1 M $HClO_4$ (pH=1.2); B) 2.99×10^{-2} M $HClO_4$+ 4.84×10^{-2} NaF (pH=2.9); under different citric acid concentrations. Scan rate 20 mV s^{-1}. The vertical line marks the position of the pzc of the unreconstructed surface.

Unlike what is observed on the Au(111) surface, the charge density vs. E curves on the Au(100) surface (Figure S2) overlap at 1.2 V, pointing to the formation of a complete adlayer during the adsorption process on this surface. In fact, according to the

corresponding Gibbs excesses, displayed in Figure 5, citrate seems to form full adlayers when adsorbs on Au(100), being the maximum coverage independent on the concentration. The maximum coverages are around 1.65×10^{14} ions cm^{-2} (pH=1) and 1.8×10^{14} ions cm^{-2} (pH=3), which correspond to coverages of 0.14 and 0.15, respectively. The Gibbs excesses behavior from pH=1 to pH=3 on Au(100) (Figure 6A) is similar to that observed on Au(111), that is, the surface excess at a constant RHE potential is higher for pH=3, implying that the number of protons exchanged during the central region of the adsorption process is larger than that of electrons, as stated in equation (1).

However, from the charge numbers displayed in Figure 6B, it can be seen that whereas the charge number fluctuates in the central region of the adsorption process moves between 2 to 2.5, it increases to 3 at the completion of the layer. This change involves a shift in the adsorption reaction, from equation (1) to a process in which 3 electrons are exchanged (similarly to what is observed on Pt(111) [16]):

$$Au+C_6H_8O_7 \rightarrow Au\text{-}C_6H_5O_7 + 3H^+ + 3e^- \qquad (2)$$

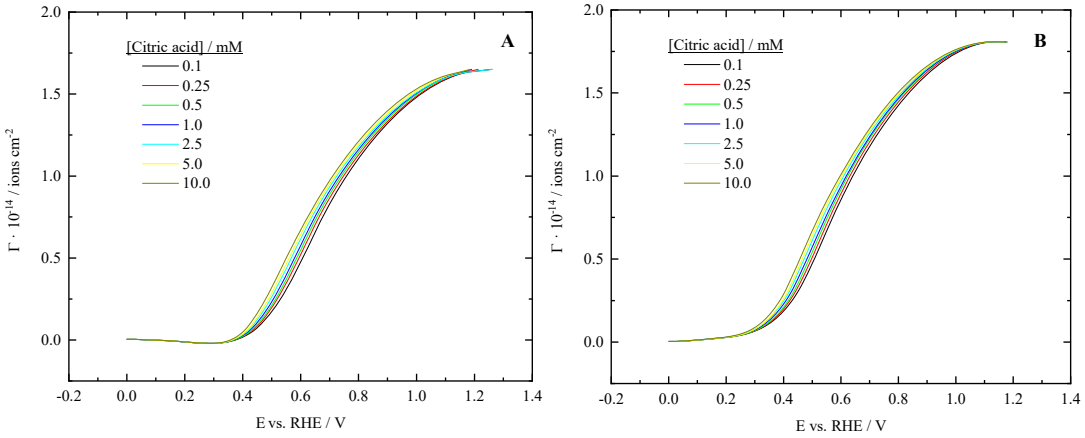

Figure 5. Gibb excesses vs. Potential of the Au(100) electrode in different solutions A) 0.1 M $HClO_4$ (pH=1.2); B) 2.99×10^{-2} M $HClO_4$+ 4.84×10^{-2} NaF (pH=2.9); under different citric acid concentrations. Scan rate 20 mV s^{-1}.

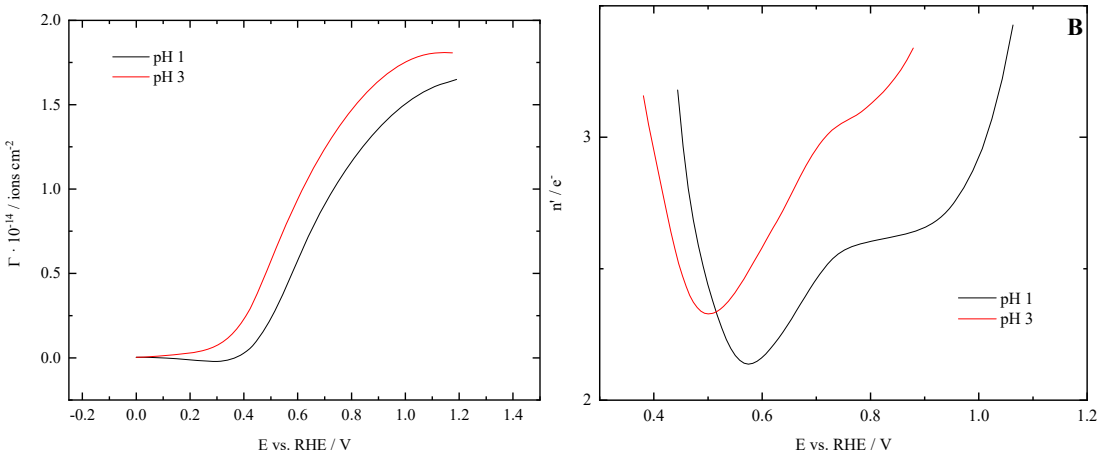

Figure 6. (A) Gibb excesses and (B) charge number vs. potential at different pHs for 10^{-3} M citric acid concentration.

3.1.3. Citrate adsorption on the Au(110) electrode.

Unlike the voltammetric profiles obtained for the Au(111) and Au(100) electrodes, the one measured for the Au(110) surface presents two peaks, being almost reversible (Figure 7). The first peak, associated with citrate adsorption, appears at ca. 0.4 V, having shoulders that are more evident for pH=3 at low potentials, and shifts to more negative potential when increasing citrate concentration. The second adsorption process is observed between 0.6 and 1.2 V, showing an ill-defined peak centered at ca. 0.95 V. The complex behavior on this surface is connected with the nature of the surface, since the (110) surface of an fcc metal is also a stepped surface exposing 1 atom-wide terraces of (111) symmetry separated by (111) monoatomic steps ((111)×(111)). Additionally, it is know that this surface also reconstructs in solution, reaching (1×2) reconstruction (or missing row reconstruction), which is lifted at positive potentials to form the (1×1) structure [55, 56].

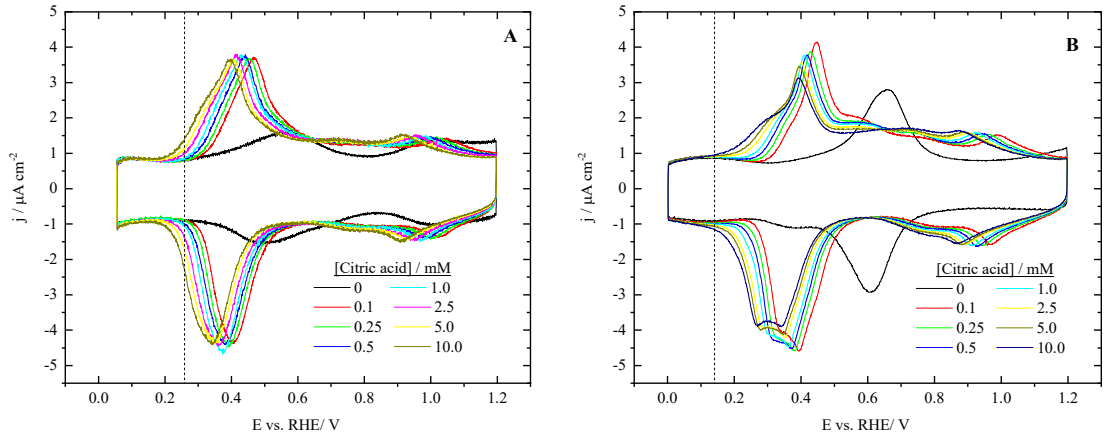

Figure 7. Voltammetric profiles of the Au(110) electrode in different solutions A) 0.1 M $HClO_4$ (pH=1.2); B) 2.99×10^{-2} M $HClO_4$+ 4.84×10^{-2} NaF (pH=2.9); under different citric acid concentrations. Scan rate 20 mV s^{-1}. The vertical line marks the position of the pzc of the unreconstructed surface.

The Gibb excesses calculated on the Au(110), from the E vs. charge density curves displayed in figure S5, clearly show that a two-step adsorption process is taking place on this surface (Figure 8). The two steps are separated by a region of nearly constant excess, which is more visible for pH=3. In the first adsorption step, between 0.2 and 0.6 V, the maximum coverage reaches the value of ca. 1.1×10^{14} ion cm^{-2}, implying that the surface coverage is ca. 0.13. After that, there is a potential region where the coverage is nearly constant, especially for pH=3. Finally, a second step, reaching surface excesses of 1.77×10^{14} ions cm^{-2} and 1.45×10^{14} ions cm^{-2} at pHs 1 and 3, corresponding to coverages of 0.2 and 0.17, respectively, takes place. It should be highlighted that the maximum coverage for pH=1 is higher than that measured for pH=3, unlike the other two electrodes (Figure 9A).

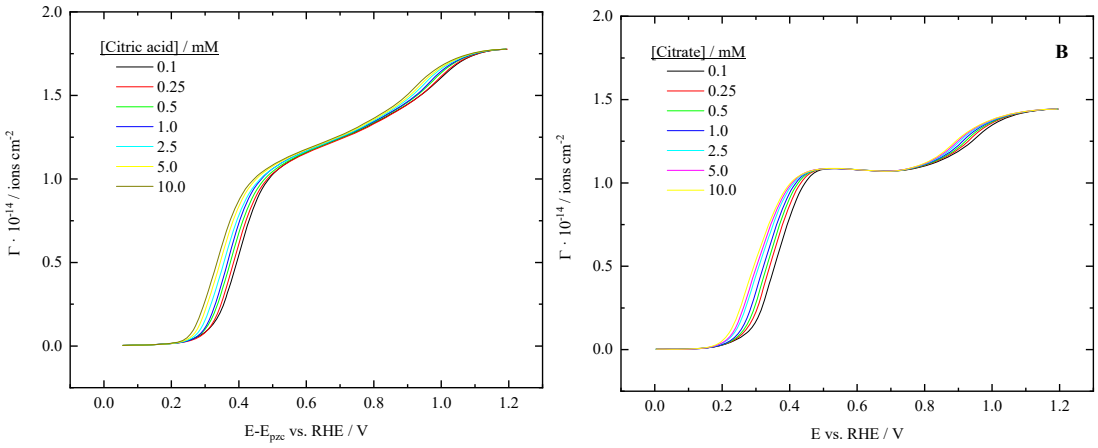

Figure 8. Gibb excesses vs. Potential of the Au(110) electrode in different solutions A) 0.1 M $HClO_4$ (pH=1.2); B) 2.99×10^{-2} M $HClO_4$+ 4.84×10^{-2} NaF (pH=2.9); under different citric acid concentrations. Scan rate 20 mV s^{-1}.

The charge numbers in the first active region, both at pHs 1 and 3, are 2 electrons (Figure 9B), indicating that citrate is being adsorbed in the form of monohydrogen citrate following the reaction:

$$Au+C_6H_8O_7 \rightarrow Au\text{-}C_6H_6O_7 + 2H^+ + 2e^- \qquad (3)$$

Nevertheless, the second adsorption process that takes place at each pH after the plateau show an increase in the charge number getting close to 2.5, which is similar to the behavior on the Au(111) surface.

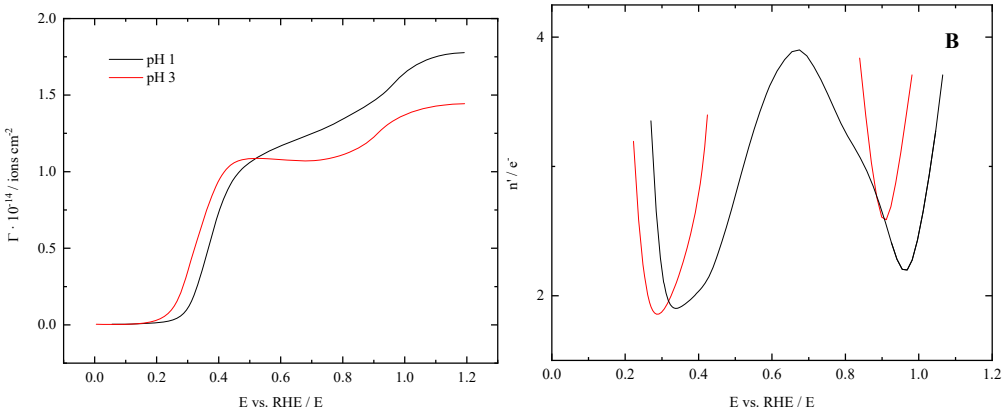

Figure 9. (A) Gibb excesses and (B) charge number vs. potential excess at different pH under citric acid 10^{-3} M.

3.2. IR results on a Au(111)-25 nm film in ATR configuration.

In order to obtain additional information on the nature of the adsorbed species, FTIR experiments were carried out. To avoid the interference of the solution species, the spectra were taken using the ATR configuration on a gold film evaporated over the prism. The deposition procedure (see methods) leads to the formation of a gold surface with a (111) preferential orientation.

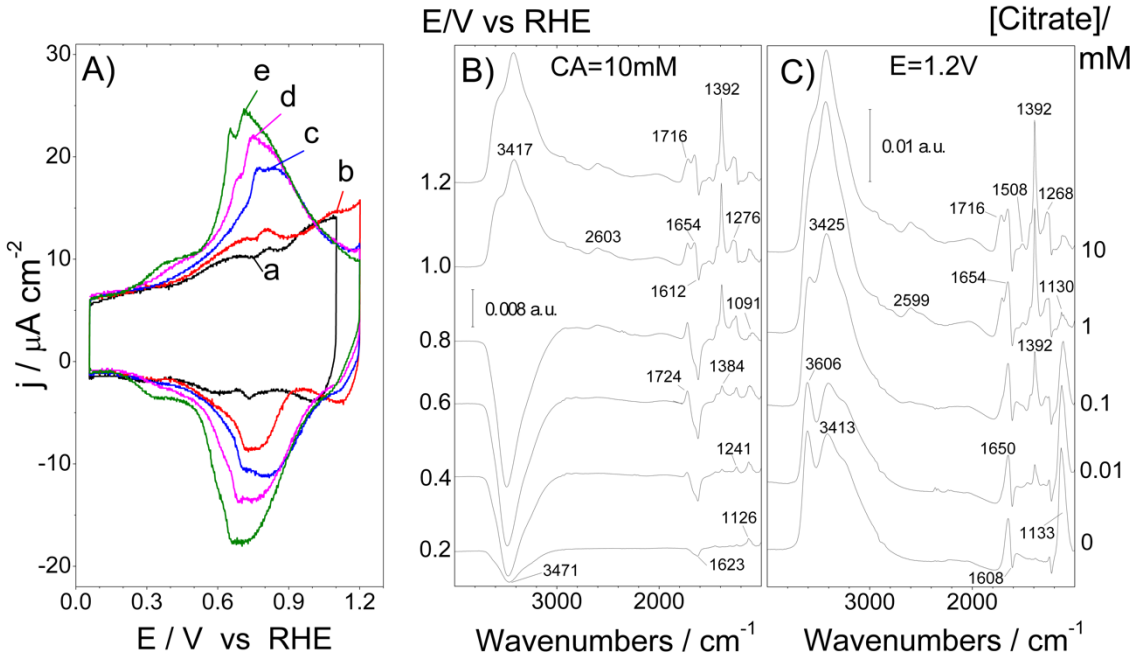

Figure 10. A) Stationary cyclic voltammograms of Au(111)-25 nm thin film electrode in contact with 0.1 M $HClO_4$ solutions containing citrate. The curves correspond to the blank electrolyte a) and with added citrate to reach concentrations equal to 0.01 mM b); 0.1 mM c); 1 mM d) and 10 mM e). Sweep rate for all curves: 50 mV s^{-1}. B) Potential-dependent ATR-SEIRAS spectra obtained for Au(111)-25nm thin film electrode in a 10 mM citrate + 0.1 M $HClO_4$ solutions. C) ATR-SEIRA spectra obtained at 1.2 V for Au(111)-25nm thin film electrode in x mM citrate + 0.1 M $HClO_4$ solutions. Reference potential 0.1 V vs RHE. 100 interferograms were collected at each potential.

The stationary cyclic voltammograms of Au(111)-25nm in contact with 0.1 M perchloric acid solutions containing citric acid with concentrations ranging from 0.01 to 10 mM are displayed in Figure 10A. The observed behavior is similar to that presented in Figure 1 for massive Au(111). Small differences are due to the higher number of defects present in the Au(111)-25 nm film. The ATR-SEIRA spectra for this electrode is shown as Figure 10B and C. Figure 10B corresponds to the potential-dependent spectra collected in a 10 mM citrate solution whereas Figure 10C shows the spectra

collected at 1.2 V in solutions with citrate concentrations ranging from 0.01 mM to ca. 10 mM.

The spectra show several bands associated to perchlorate, citrate, and water interacting with the surface. The band at 1100-1130 cm^{-1} can be assigned to the asymmetrical tension of the Cl-O binding (as ClO_4) of adsorbed perchlorate [57, 58]. Moreover, it is expected that citrate species compete with perchlorate for the adsorption sites, which can be observed in Figure 10C, where the intensity of the band at 1133 cm^{-1} diminishes as the citrate concentration increases.

Citrate adsorption takes place usually through the carboxylic groups [59], involving their deprotonation. Carboxylic groups in solution exhibits asymmetric and symmetric stretching vibration bands which appear typically around 1500-1630 cm^{-1} and 1305-1415 cm^{-1}, respectively. However, as has been observed for other species having carboxylic groups (oxalate, acetate), citrate species adsorb on gold through both of the oxygen atoms, of each involved carboxylic group, in a bidentate configuration, leaving the C-C axis perpendicular to the surface (η2-COO-bridging). Under this configuration, the dynamic dipole for the asymmetric stretching vibration (asO-C-O mode) is parallel to the electrode surface, and the corresponding band cannot be observed in the spectra, as a result of the surface selection rule [60, 61]. Therefore, independently of the citrate coverage, no asymmetric O-C-O band appears between 1500-1600 cm^{-1}. This behavior was also observed by Floate et al. on Au(111) [18]. On the other hand, the band at ca. 1392 cm^{-1}, assigned to the symmetric O-C-O vibrational mode, shows the expected behavior: increase with the electrode potential (Figure 10B) and citrate concentration (Figure 10C).

Regarding the dependence on the potential of the vibrational properties of interfacial water molecules, the stretching ν(OH) and bending δ(OH) of the OH bonds

of the water molecule appear between 3600-3000 and 1650-1610 cm^{-1}, respectively. At potentials below the potential of zero charge (E_{pzc}=0.55 V [23]), negative bands around 3470 and 1612 cm^{-1} are observed. These bands are displaced at higher and lower frequencies, respectively, with respect to those observed in the liquid water spectrum [62]. These bands are due to weakened water molecules as they are oriented with hydrogen atoms towards the metal surface when it is negatively charged. At $E>E_{pzc}$, a wideband at 3400 cm^{-1} is observed, attributed to the tension of the binding OH (which are interacting with other water molecules) [63]. The weak band observed at 3606 cm^{-1}, which appears at 0.6-0.7 V, which also increases with the applied potential, is due to the unbound OH tension very close to the perchlorate anions. A positive band around 3650 cm^{-1} (not shown) (E=0.8-0.9 $V>E_{pzc}$) can be attributed to isolated water molecules between citrate anions. The presence of this band suggests that the adsorbed citrate anions at low coverages partially break the interfacial water network, hindering the interaction of perchlorate anions with the electrode. The change in the sign of the bands above 1.0 V may be related to changes in the binding mode of water upon completion of the adlayer or the incipient OH adsorption on the surface at the highest potential values.

Increasing the potential in the positive scan direction, additional positive bands at 2600, 1716, 1508, 1270 and 1091 cm^{-1} appear, whose intensity increases with potential and coverage. The small peaks at 3000 and 2600 cm^{-1} could be attributed to O-H stretching between hydrogen-bonded carboxylic acid groups [64, 65]. Max et al. assigned the bands between 3000 and 2600 cm^{-1} to carboxylic OH groups hydrogen-bonded to either other carboxylic groups or water molecules. Moreover, Martin et al. suggested the formation of oxalic acid dimers during the adsorption of oxalic acid onto Cu (110) surfaces under UHV conditions [65]. In this case, the existence of these bands should be related to the presence of undissociated carboxylic groups in the interphase.

Thus, these small peaks at 3000 and 2600 cm^{-1} are connected with the appearance of the band at 1704 cm^{-1}, which is assigned to hydrogen bonding in carboxylic groups. Delgado et al. assigned the 1704 cm^{-1} band to the ν(C-O) mode of succinate ($^{-}OOCCH2CH2COO^{-}$)[65], which suggests the formation of COOH hydrogen bonding between adsorbed succinate anions, supporting the hydrogen bonding through terminal COOH groups between neighboring citrate species [66].

Bands are also observed at 1508, 1260, and 1090 cm^{-1} at high potential and high coverage. The band to 1508 cm^{-1} could be attributed to O-H in-plane bending, which appears only under acidic condition [64], being this vibration band the characteristic coordination of the alcoholic oxygen atom of citrate to a metal ion [67]. The band at ca. 1260 cm^{-1} could be tentatively related to the ν(C-OH) + δ(C-O-H) band as observed in adsorbed bioxalate [68, 69].

As final thoughts, it can be pointed out, that the presence of citrate anions and hydrogen bonding between free COOH groups could contribute to the formation of multiple citrate layers on the surface, and that the electric field (applied potential) may contract the citrate layer leading to a slightly smaller thickness [70]. The combination of the FTIR and thermodynamic analysis indicates that citrate is deprotonated upon adsorption and the free carboxylic groups not bonded to the surface have hydrogen bonds with additional citric acid molecules. These results are in agreements with previous results on the adsorption of citrate using external reflection FTIR on Au(111) electrodes which suggested that citrate was fully deprotonated upon adsorption [71].

3.3. DFT adsorption calculations of citrate on gold

To value the experimentally derived insights for citrate adsorption on gold, chemisorbed states of citrate on the different basal planes of gold (Au(100), Au(110)

and Au(111)) where searched using DFT. Adsorbed citrate configurations bonded to the surface through one, two and three carboxylic groups, each one of them in bidentate configuration, with the adsorbate main chain laying parallel to the surface, were considered, as suggested by the FTIR spectra (no vibrational modes other than those related to the carboxylic group in bidentate configuration where detected for the adsorbate). Since each adsorbed carboxylic group in bidentate configurations involves its deprotonation, giving rise to a proton-coupled electron transfer (PCET), free energies (ΔG) and equilibrium potentials (E), for the most relevant configurations, were calculated according to the electrode reactions:

$$Au+C_6H_8O_7 \rightarrow Au\text{-}C_6H_7O_7+1/2H_2 \quad (4)$$

$$Au+C_6H_8O_7 \rightarrow Au\text{-}C_6H_6O_7+H_2 \quad (5)$$

$$Au+C_6H_8O_7 \rightarrow Au\text{-}C_6H_5O_7+3/2H_2 \quad (6)$$

The most favorable adsorbent/adsorbate configuration found after each number of PCTEs on each basal plane is shown in table S1, meanwhile the corresponding energetics and potentials are summarized in Table 1. Additionally, the most relevant configurations of citrate adsorbed on each basal plane of gold (that binding the higher number possible of deprotonated carboxylic groups to the surface in bidentate configuration) are displayed in Figure 11.

Table 1. Energetics (free energy ΔG and electrode potential E) of the adsorption processes of citrate on the different basal planes of gold after one, two and three proton-coupled electron transfers (PCETs) under the dehydrogenated carboxylic groups bonded to the surface in bidentate configuration conditions.

	Au(100)		Au(110)		Au(111)	
	ΔG/eV	E/V	ΔG/eV	E/V	ΔG/eV	E/V
1 PCET	0.41	0.41	0.07	0.07	0.26	0.26
2 PCETs	1.36	0.68	0.41	0.21	1.35	0.68
3 PCETs					2.68	0.89

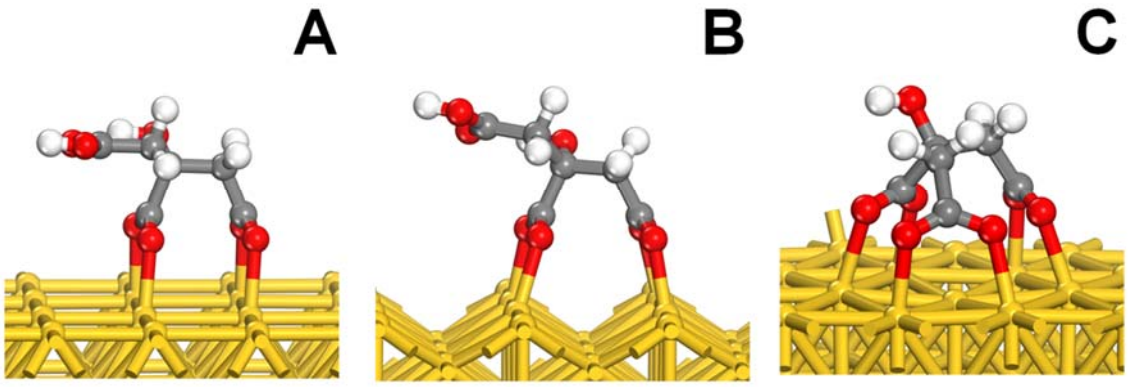

Figure 11. Adsorbed citrate on (A) Au(100), (B) Au(110) and (C) Au(111) for the most favorable configuration found binding the higher number possible of carboxylic groups to the surface in bidentate configuration.

From Table 1, it can be concluded that, according to these DFT results, citrate can become simultaneously bonded to the surface through two deprotonated carboxylic groups in bidentate configuration on each one of the basal planes of gold, being the simultaneous bonding through the three deprotonated carboxylic groups in bidentate configuration only possible on the Au(111) plane. At low potentials, in the order of 0.07, 0.26 and 0.41 V for the Au(110), Au(111) and Au(100), respectively, only a single PCET per adsorbed citrate can occur. Thus, at low potentials, citrate can become adsorbed on each basal plane of gold only through a single carboxylic group in bidentate configuration, following the activity order Au(110)>Au(111)>Au(100). As the potential increases, from 0.68 V for the Au(111) and Au(100) and from 0.41 V for the Au(110), the adsorption of citrate through two deprotonated carboxylic groups in bidentate configuration becomes possible on each one of the basal planes of gold.

Finally, at higher potentials than 0.98 V, citrate adsorption through three deprotonated carboxylic groups in bidentate configuration becomes possible only on the Au(111) surface, as was also found for the Pt(111) surface [16]. The adsorption behavior difference between Au(100) and Au(110) and that on A(111) is probably related to the rigidity of the backbone of the adsorbate, which is not able to accommodate its geometry to the layouts of the gold atoms exposed by the Au(100) and

Au(110) surfaces, so that the third deprotonated carboxylic group is bonded in the bidentate configuration.

Thus, the adsorption behavior of citrate on single crystal gold electrodes would be qualitatively the same than that found on single crystal platinum electrodes, though the potentials at which each configuration would be favorable are significantly lower for platinum, which is a clear manifestation of the stronger bonding of citrate species to platinum.

3.4. Relationship between citrate adsorption behavior on gold and shape of colloidal gold NPs.

The adsorption behavior of citrate on gold under the synthesis of colloidal AuNPs in water conditions can be reliably determined from the reported adsorption behavior of citrate on gold under electrochemical conditions, complemented by FTIR spectra and DFT calculations. On the one side, the whole of the reported results points to that citrate can become simultaneously adsorbed through two deprotonated carboxylic groups in bidentate configuration on each one of the basal planes of gold under the synthesis conditions of colloidal AuNPs in water. Pieces of evidence supporting this assessment are multiple. First, it has been observed that adsorption processes give rise to lower pK_a values for adsorbed acids, favoring their deprotonation [72]. Second, the charge numbers measured in the potential region where a significant charge excess change was observed are close to 2 for the three basal planes. Third, plausible chemisorbed states of citrate after two PCETs under the pre-established conditions were found for each plane using DFT. Finally, the potential regions where charge numbers close to 2 were measured coincide with those where the citrate adsorption through two deprotonated carboxylic groups in bidentate configuration was

found to be possible for each plane using DFT. Thus, experimental and computational results reinforce mutually. According to the experiments, the adsorbate coverages at the potentials under which the citrate adsorption through two deprotonated carboxylic groups in bidentate configuration becomes possible would be still low, on each basal plane.

On the other side, DFT calculations provide evidence that citrate can become simultaneously adsorbed through three dehydrogenated carboxylic groups in bidentate configuration only on the Au(111) surface, at high potentials. In spite of that, this adsorption mode was not detected either by the thermodynamic analysis or in the FTIR spectra. The adsorption behavior difference between the Au(111) and the Au(100) and Au(110) surfaces would be related to the rigidity of the backbone of the adsorbate, which would be not able to accommodate its geometry to the layouts of the atoms exposed by the Au(100) and Au(110) surfaces, so that third dehydrogenated group cannot be bonded under the bidentate configuration. It should be mentioned that the stable configuration is determined for a single molecule in the unit cell. The presence of neighboring citrate molecules or water can alter the energetics of the process, destabilizing the adsorption through the three carboxylic groups.

In any case, the citrate adsorption on the Au(111) surface through three deprotonated carboxylic groups in bidentate configuration would become favorable only at high coverages. Probably, this transformation is not observed experimentally (the measured charge number is close to two) because it takes place at high potentials, which can be translated to a preferential adsorption on Au(111) crystallographic facets. Also, surface excesses at E>0.7 V follow the order Au(111)>Au(110)>Au(100) as can be observed in figure S6. This implies that the Au(111) surface has the strongest interactions with citrate, because the coverages are significantly higher. Therefore, by

controlling the kinetics of the reduction of $AuCl_4^-$ for the synthesis of AuNPs, citrate can direct the growth of the Au nanoseeds with the formation of (111) facets. The control of the kinetics can be achieved by the use of a mild reducing agent, i.e., citrate, which should be able to maintain the reduction potential above 0.7 V, so that adsorption on the {111} facet is preferred over the other two possible orientations. Tetrahedral and octahedral forms will arise from the {111} 3-dimentional growth of the AuNPs.

4. Conclusions

To engineer colloidal methods of synthesis and capping agents capable of producing metal nanoparticles (NPs) of specific shape and size, knowledge about mechanisms have to be improved. These mechanisms are actually driven by the adsorption behavior of the involved species on the surfaces exposed by the growing NPs. Combining electrochemical experiments, FTIR spectra ad DFT calculations on well-defined surfaces, the adsorption behavior of citrate on the three basal planes of gold in water is here characterized. DFT results indicate that citrate can be simultaneously adsorbed on Au(111) through three dehydrogenated carboxylic groups, each of them in bidentate configuration, instead of only two on Au(100) and Au(110) under the synthesis conditions. This adsorption behavior suggests that citrate is stronger adsorbed on Au(111) than on other two basal planes, which would explain why tetrahedral and octahedral colloidal AuNPs are preferentially shaped when citric acid is used as the capping agent in water. Moreover, FTIR results would indicate that, when citrate is adsorbed on gold through only two dehydrogenated carboxylic groups, the third one would favor the formation of a bilayer via hydrogen-bonding. This insight would be consistent with the thermodynamic data, pointing mostly to 2 as charge number in the

active region of the adsorption processes. In any case, further studies would be needed to completely understand the shaping mechanism.

Although a deep fundamental study has been carried out to understand the citrate adsorption on the gold basal planes, further studies need to be achieved to understand accurately the reason why the citrate is preferentially adsorbed during the nucleation process of AuNPs synthesis, so guiding to the final shape of the nanoparticles.

Acknowledgements

This work has been financially supported by the MCINN-FEDER (Spain) through project CTQ2016-76221-P.

References

[1] F.J. Vidal-Iglesias, J. Solla-Gullón, P. Rodríguez, E. Herrero, V. Montiel, J.M. Feliu, A. Aldaz, Shape-dependent electrocatalysis: Ammonia oxidation on platinum nanoparticles with preferential (100) surfaces, Electrochem. Commun., 6 (2004) 1080-1084.
[2] P.K. Jain, I.H. El-Sayed, M.A. El-Sayed, Au nanoparticles target cancer, Nano Today, 2 (2007) 18-29.
[3] P.F. Jiao, H.Y. Zhou, L.X. Chen, B. Yan, Cancer-targeting multifunctionalized gold nanoparticles in imaging and therapy, Current Medicinal Chemistry, 18 (2011) 2086-2102.
[4] J. Peng, X. Liang, Progress in research on gold nanoparticles in cancer management, Medicine, 98 (2019) e15311.
[5] P. Singh, S. Pandit, V.R.S.S. Mokkapati, A. Garg, V. Ravikumar, I. Mijakovic, Gold nanoparticles in diagnostics and therapeutics for human cancer, International Journal of Molecular Sciences, 19 (2018) 1979.
[6] C.Q. Sun, B.K. Tay, X.T. Zeng, S. Li, T.P. Chen, J. Zhou, H.L. Bai, E.Y. Jiang, Bond-order bond-length bond-strength (bond-ols) correlation mechanism for the shape-and-size dependence of a nanosolid, Journal of Physics: Condensed Matter, 14 (2002) 7781-7795.
[7] D. Zanchet, H. Tolentino, M.C. Martins Alves, O.L. Alves, D. Ugarte, Inter-atomic distance contraction in thiol-passivated gold nanoparticles, Chemical Physics Letters, 323 (2000) 167-172.
[8] M.T.M. Koper, Structure sensitivity and nanoscale effects in electrocatalysis, Nanoscale, 3 (2011) 2054-2073.
[9] M. Haruta, When gold is not noble: Catalysis by nanoparticles, The Chemical Record, 3 (2003) 75-87.
[10] Y. Li, E. Boone, M.A. El-Sayed, Size effects of pvp−pd nanoparticles on the catalytic suzuki reactions in aqueous solution, Langmuir, 18 (2002) 4921-4925.

[11] A.J. Bard, Inner-sphere heterogeneous electrode reactions. Electrocatalysis and photocatalysis: The challenge, J. Am. Chem. Soc., 132 (2010) 7559-7567.
[12] S. Link, M.A. El-Sayed, Size and temperature dependence of the plasmon absorption of colloidal gold nanoparticles, The Journal of Physical Chemistry B, 103 (1999) 4212-4217.
[13] J. Turkevich, P.C. Stevenson, J. Hillier, A study of the nucleation and growth processes in the synthesis of colloidal gold, Discussions of the Faraday Society, 11 (1951) 55-75.
[14] G. Frens, Controlled nucleation for the regulation of the particle size in monodisperse gold suspensions, Nature Physical Science, 241 (1973) 20.
[15] G.A. Attard, J.Y. Ye, P. Jenkins, F.J. Vidal-Iglesias, E. Herrero, S.G. Sun, Citrate adsorption on pt{hkl} electrodes and its role in the formation of shaped pt nanoparticles, J. Electroanal. Chem., 688 (2013) 249-256.
[16] J.M. Gisbert-Gonzalez, J.M. Feliu, A. Ferre-Vilaplana, E. Herrero, Why citrate shapes tetrahedral and octahedral colloidal platinum nanoparticles in water, J. Phys. Chem. C, 122 (2018) 19004-19014.
[17] Y. Lin, G.-B. Pan, G.-J. Su, X.-H. Fang, L.-J. Wan, C.-L. Bai, Study of citrate adsorbed on the au(111) surface by scanning probe microscopy, Langmuir, 19 (2003) 10000-10003.
[18] S. Floate, M. Hosseini, M.R. Arshadi, D. Ritson, K.L. Young, R.J. Nichols, An in-situ infrared spectroscopic study of the adsorption of citrate on au(111) electrodes, J. Electroanal. Chem., 542 (2003) 67-74.
[19] J. Kunze, I. Burgess, R. Nichols, C. Buess-Herman, J. Lipkowski, Electrochemical evaluation of citrate adsorption on au(111) and the stability of citrate-reduced gold colloids, Journal of Electroanalytical Chemistry, 599 (2007) 147-159.
[20] A. Rodes, E. Herrero, J.M. Feliu, A. Aldaz, Structure sensitivity of irreversibly adsorbed tin on gold single-crystal electrodes in acid media, Journal of the Chemical Society-Faraday Transactions, 92 (1996) 3769-3776.
[21] A. Berna, J.M. Delgado, J.M. Orts, A. Rodes, J.M. Feliu, Spectroelectrochemical study of the adsorption of acetate anions at gold single crystal and thin-film electrodes, Electrochim. Acta, 53 (2008) 2309-2321.
[22] J.M. Delgado, J.M. Orts, J.M. P,rez, A. Rodes, Sputtered thin-film gold electrodes for in situ atr-seiras and sers studies, Journal of Electroanalytical Chemistry, 617 (2008) 130-140.
[23] T. Wandlowski, K. Ataka, S. Pronkin, D. Diesing, Surface enhanced infrared spectroscopy - au(1 1 1-20 nm)/sulphuric acid - new aspects and challenges, Electrochim. Acta, 49 (2004) 1233-1247.
[24] A. Rodes, Pérez, J. M., Aldaz, A, Vibrational spectroscopy, in: W.L. Vielstich, Arnold, Gasteiger, H. A. (Ed.) Handbook of fuel cells - fundamentals, technology and applications, John Wiley & Sons, Ltd, Chichester, 2003.
[25] B. Delley, An all-electron numerical method for solving the local density functional for polyatomic molecules, J. Chem. Phys., 92 (1990) 508-517.
[26] B. Delley, Hardness conserving semilocal pseudopotentials, Phys. Rev. B, 66 (2002) 155125.
[27] J.P. Perdew, K. Burke, M. Ernzerhof, Generalized gradient approximation made simple [phys. Rev. Lett. 77, 3865 (1996)], Phys. Rev. Lett., 78 (1997) 1396-1396.
[28] B. Hammer, L.B. Hansen, J.K. Nørskov, Improved adsorption energetics within density-functional theory using revised perdew-burke-ernzerhof functionals, Phys. Rev. B, 59 (1999) 7413-7421.
[29] B. Delley, From molecules to solids with the dmol(3) approach, Journal of Chemical Physics, 113 (2000) 7756-7764.
[30] A. Tkatchenko, M. Scheffler, Accurate molecular van der waals interactions from ground-state electron density and free-atom reference data, Phys. Rev. Lett., 102 (2009) 073005.
[31] B. Delley, The conductor-like screening model for polymers and surfaces, Mol. Simulat., 32 (2006) 117-123.

[32] J. Neugebauer, M. Scheffler, Adsorbate-substrate and adsorbate-adsorbate interactions of na and k adlayers on al(111), Phys. Rev. B, 46 (1992) 16067-16080.
[33] J.K. Nørskov, J. Rossmeisl, A. Logadottir, L. Lindqvist, J.R. Kitchin, T. Bligaard, H. Jónsson, Origin of the overpotential for oxygen reduction at a fuel-cell cathode, J. Phys. Chem. B, 108 (2004) 17886-17892.
[34] S. Narasimhan, D. Vanderbilt, Elastic stress domains and the herringbone reconstruction on au(111), Physical Review Letters, 69 (1992) 1564-1567.
[35] U. Harten, A.M. Lahee, J.P. Toennies, C. Wöll, Observation of a soliton reconstruction of au(111) by high-resolution helium-atom diffraction, Physical Review Letters, 54 (1985) 2619-2622.
[36] R.J. Needs, M. Mansfield, Calculations of the surface stress tensor and surface energy of the (111) surfaces of iridium, platinum and gold, Journal of Physics: Condensed Matter, 1 (1989) 7555-7563.
[37] D.M. Kolb, Reconstruction phenomena at metal-electrolyte interfaces, Prog. Surf. Sci., 51 (1996) 109-173.
[38] D.M. Kolb, J. Schneider, Surface reconstruction in electrochemistry: Au(100-(5 × 20), au(111)-(1 × 23) and au(110)-(1 × 2), Electrochimica Acta, 31 (1986) 929-936.
[39] O.M. Magnussen, J. Hageböck, J. Hotlos, R.J. Behm, In situ scanning tunnelling microscopy observations of a disorder–order phase transition in hydrogensulfate adlayers on au(111), Faraday Discussions, 94 (1992) 329-338.
[40] Z. Shi, J. Lipkowski, M. Gamboa, P. Zelenay, A. Wieckowski, Investigations of so42− adsorption at the au(111) electrode by chronocoulometry and radiochemistry, Journal of Electroanalytical Chemistry, 366 (1994) 317-326.
[41] X. Gao, S.C. Chang, X. Jiang, A. Hamelin, M.J. Weaver, Emergence of atomic level structural information for oredered metal-solution interfaces : Some recent contributions from in- situ infrared spectroscopy and scanning tunneling microscopy, Journal of Vacuum Science and Technology A, 10 (1992) 2972.
[42] A. Hamelin, L. Stoicoviciu, G.J. Edens, X. Gao, M.J. Weaver, Some electrochemical consequences of potencial-induced surface reconstruction on au(100): Double layer nonuniformity and electrode kinetics, J. Electroanal. Chem., 365 (1994) 47-57.
[43] J. Schneider, D.M. Kolb, Potential-induced surface reconstruction of au(100), Surface Science, 193 (1988) 579-592.
[44] X. Gao, A. Hamelin, M.J. Weaver, Atomic relaxation at ordered electrode surfaces probed by scanning tunneling microscopy: Au(111) in aqueous solution compared with ultrahigh-vacuum environments, The Journal of Chemical Physics, 95 (1991) 6993-6996.
[45] U.W. Hamm, D. Kramer, R.S. Zhai, D.M. Kolb, The pzc of au(111) and pt(111) in a perchloric acid solution: An ex situ approach to the immersion technique, J. Electroanal. Chem., 414 (1996) 85-89.
[46] D.M. Kolb, J. Schneider, Surface reconstuction in electrochemistry: Au(100)-(5x20), au(111)-(1x23) and au(110)-(1x2), Electrochim. Acta, 31 (1986) 929-936.
[47] A. Chen, J. Lipkowski, Electrochemical and spectroscopic studies of hydroxide adsorption at the au(111) electrode, The Journal of Physical Chemistry B, 103 (1999) 682-691.
[48] J. Lipkowski, Z. Shi, A. Chen, B. Pettinger, C. Bilger, Ionic adsorption at the au(111) electrode, Electrochimica Acta, 43 (1998) 2875-2888.
[49] Z. Shi, J. Lipkowski, S. Mirwald, B. Pettinger, Electrochemical and second harmonic generation study of so2−4 adsorption at the au(111) electrode, Journal of Electroanalytical Chemistry, 396 (1995) 115-124.
[50] Z. Shi, J. Lipkowski, Chloride adsorption at the au(111) electrode surface, Journal of Electroanalytical Chemistry, 403 (1996) 225-239.
[51] M.A. Van Hove, R.J. Koestner, P.C. Stair, J.P. Bibérian, L.L. Kesmodel, I. BartoŠ, G.A. Somorjai, The surface reconstructions of the (100) crystal faces of iridium, platinum and gold: I.

Experimental observations and possible structural models, Surface Science, 103 (1981) 189-217.
[52] X.P. Gao, A. Hamelin, M.J. Weaver, Potential-dependent reconstruction at ordered au(100)-aqueous interfaces as probed by atomic-resolution scanning tunneling microscopy, Physical Review Letters, 67 (1991) 618-621.
[53] X.P. Gao, A. Hamelin, M.J. Weaver, Elucidating complex surface reconstructions with atomic-resolution scanning tunneling microscopy - au(100)-aqueous electrochemical interface, Physical Review B, 46 (1992) 7096-7102.
[54] U.W. Hamm, D.M. Kolb, On the stability of reconstructed au(100) surfaces in the presence of organic molecules, Journal of Electroanalytical Chemistry, 332 (1992) 339-347.
[55] G. Binnig, H. Rohrer, C. Gerber, E. Weibel, (111) facets as the origin of reconstructed au(110) surfaces, Surface Science Letters, 131 (1983) L379-L384.
[56] X.P. Gao, A. Hamelin, M.J. Weaver, Reconstruction at ordered au(110)-aqueous interfaces as probed by atomic-resolution scanning tunneling microscopy, Physical Review B, 44 (1991) 10983-10986.
[57] G. Herzberg, B.L. Crawford, Infrared and raman spectra of polyatomic molecules, The Journal of Physical Chemistry, 50 (1946) 288-288.
[58] J.J. Calvante, N.S. Marinković, Z. Kováčová, W. Ronald Fawcett, Sniftirs studies of the double layer at the metal/solution interface. Part 1. Single crystal gold electrodes in aqueous perchloric acid, Journal of Electroanalytical Chemistry, 421 (1997) 49-57.
[59] R.B. Martin, A complete ionization scheme for citric acid, The Journal of Physical Chemistry, 65 (1961) 2053-2055.
[60] R.G. Greenler, Infrared study of adsorbed molecules on metal surfaces by reflection techniques, J. Chem. Phys., 44 (1966) 310-315.
[61] M. Osawa, K.-I. Ataka, K. Yoshii, Y. Nishikawa, Surface-enhanced infrared spectroscopy: The origin of the absorption enhancement and band selection rule in the infrared spectra of molecules adsorbed on fine metal particles, Applied Spectroscopy, 47 (1993) 1497-1502.
[62] S. J.R., in: Clark, H.R.E. R.J.H. (Eds.) Advances
in infrared and raman spectroscopy, Heyser, London, 1978, pp. 149-216.
[63] K.-i. Ataka, T. Yotsuyanagi, M. Osawa, Potential-dependent reorientation of water molecules at an electrode/electrolyte interface studied by surface-enhanced infrared absorption spectroscopy, The Journal of Physical Chemistry, 100 (1996) 10664-10672.
[64] J.-W. Park, J.S. Shumaker-Parry, Structural study of citrate layers on gold nanoparticles: Role of intermolecular interactions in stabilizing nanoparticles, Journal of the American Chemical Society, 136 (2014) 1907-1921.
[65] D.S. Martin, R.J. Cole, S. Haq, Investigating the adsorption of oxalic acid onto cu(110) to create a chemically functionalised surface, Surface Science, 539 (2003) 171-181.
[66] J.M. Delgado, A. Berná, J.M. Orts, A. Rodes, J.M. Feliu, In situ infrared study of the adsorption and surface acid−base properties of the anions of dicarboxylic acids at gold single crystal and thin-film electrodes, The Journal of Physical Chemistry C, 111 (2007) 9943-9952.
[67] A. Heller, A. Barkleit, H. Foerstendorf, S. Tsushima, K. Heim, G. Bernhard, Curium(iii) citrate speciation in biological systems: A europium(iii) assisted spectroscopic and quantum chemical study, Dalton Transactions, 41 (2012) 13969-13983.
[68] A. Berná, A. Rodes, J.M. Feliu, An in situ infrared and electrochemical study of oxalic acid adsorption at stepped platinum single crystal electrodes in the [0$\bar{1}$1] zone, Electrochimica Acta, 49 (2004) 1257-1269.
[69] A. Berná, A. Rodes, J.M. Feliu, Oxalic acid adsorption and oxidation at platinum single crystal electrodes, Journal of Electroanalytical Chemistry, 563 (2004) 49-62.
[70] M. Giersig, P. Mulvaney, Preparation of ordered colloid monolayers by electrophoretic deposition, Langmuir, 9 (1993) 3408-3413.
[71] R.J. Nichols, I. Burgess, K.L. Young, V. Zamlynny, J. Lipkowski, A quantitative evaluation of the adsorption of citrate on au(111) using sniftirs, J. Electroanal. Chem., 563 (2004) 33-39.

[72] R. Martínez-Hincapie, A. Berna, A. Rodes, V. Climent, J.M. Feliu, Surface acid-base properties of anion-adsorbed species at pt(111) electrode surfaces in contact with co2-containing perchloric acid solutions, J. Phys. Chem. C, 120 (2016) 16191-16199.